Electron Microscopic Reconstruction of Neural Circuitry in the Cochlea

Yunfeng Hua[1-5*#], Xu Ding[2-4*], Haoyu Wang[4*], Yunge Gao[2,3], Fangfang Wang[4], Tobias Moser[6-8#], Hao Wu[1-4#]

[1]Department of Otolaryngology-Head and Neck Surgery, Shanghai Ninth People's Hospital, China
[2]Ear Institute, Shanghai Jiao Tong University School of Medicine, China
[3]Shanghai Key Laboratory of Translational Medicine on Ear and Nose Diseases, China
[4]Shanghai Institute of Precision Medicine, Shanghai Ninth People's Hospital, China
[5]Department of Connectomics, Max-Planck-Institute for Brain Research, Germany
[6]Institute for Auditory Neuroscience, University Medical Center Göttingen, 37075 Göttingen, Germany
[7]Auditory Neuroscience Group, Max Planck Institute of Experimental Medicine, 37075 Göttingen, Germany
[8]Multiscale Bioimaging Cluster of Excellence (MBExC), University of Göttingen, 37075 Göttingen, Germany

*These authors contributed equally to this work.
[#]Correspondence: haowu@sh-jei.org (H.W.), yunfeng.hua@shsmu.edu.cn (Y.H.), tmoser@gwdg.de (T.M.)

Abstract

Recent studies have revealed great diversity in the structure, function and efferent innervation of afferent synaptic connections between the cochlear inner hair cells (IHCs) and spiral ganglion neurons (SGN), which likely enables audition to cover a wide range of sound pressures. By performing an extensive electron microscopic reconstruction of the neural circuitry in the mature mouse organ of Corti, we demonstrate that afferent SGN fibers differ in strength and composition of efferent innervation in a manner dependent on their synaptic connectivity with IHCs. SGNs that sample glutamate release from several presynaptic ribbons receive more efferent innervation from lateral olivocochlear projections than those driven by a single ribbon. Next to the prevailing unbranched SGNs, we found branched SGNs that can contact several IHCs. Unexpectedly, medial

olivocochlear neurons provide efferent SGN innervation with a preference for single ribbon, pillar synapses. We conclude that afferent and efferent innervations of SGNs are tightly matched.

Introduction

Acoustic information is encoded into electrical signals in the cochlea, the mammalian hearing organ in the inner ear. Sound encoding by afferent spiral ganglion neurons (SGN) faithfully preserves signal features such as frequency, intensity, and timing (for reviews see ref. 1-3). It also is tightly modulated by efferent projections of the central nervous system to enable selective attention and to aid signal detection in noisy background, sound source localization as well as ear protection against acoustic trauma (see reviews[4,5]). The sound encoding occurs at the afferent connections between inner hair cells (IHCs) and postsynaptic type-1 SGNs (^{1}SGNs) that constitute 95% of all SGNs[6,7]. These so called ribbon synapses mediate glutamate-mediated neurotransmission at extraordinary high rates and with great temporal precision[1,8]. The electron-dense presynaptic ribbon i) tethers dozens of synaptic vesicles (SVs), ii) enables indefatigable SV replenishment of the large readily releasable SV pool and iii) organizes Ca^{2+} channels at the active zones (AZs) of IHCs[9-12].

In the mammalian cochlea, each IHC is contacted by 10-30 ^{1}SGNs, whereby predominantly an AZ with a single ribbon drives firing in a single unbranched peripheral dendrite. These afferent connections exhibit great diversity in synaptic and ^{1}SGN dendritic morphology[13-20], physiological properties[6,13,16,17,20-24], and molecular ^{1}SGN profile[25-27]. What might appear as a peculiar biological variance at first glance, is becoming increasingly recognized as a fascinating parallel information processing mechanism by which the auditory system copes with encoding over a broad range of sound pressures downstream of cochlear micromechanics. Specifically, emerging evidence indicates that the full sound intensity information contained in the IHC receptor potential is fractionated into subpopulations of ^{1}SGNs that collectively encode the entire audible range of ^{1}SGNs (reviewed in ref. 1,28-30). The synaptic and neural diversity shows an interesting pattern of spatial organization.

55 [1]SGNs with low spontaneous firing rate and high sound threshold primarily contact the modiolar
56 face of the IHCs[6]. There, AZs contain larger and/or multiple ribbons as well as more membrane-
57 proximal SVs and Ca^{2+} channels that need stronger depolarization for activation than at the pillar
58 face, which is contacted by [1]SGNs with high spontaneous firing rate and low sound threshold.
59 Afferent signaling is dynamically modulated by two distinct efferent projections emanating from
60 the medial and lateral superior olivary complex of the auditory brainstem[31]. It is generally thought
61 that the lateral olivocochlear component (LOC) directly modulates [1]SGNs by efferent synapses near
62 the ribbon synapses of the peripheral [1]SGN neurites (also referred to as dendrites, for reviews see
63 ref. 5,32). Efferent innervation seems more pronounced for [1]SGNs contacting IHCs at the modiolar
64 face and de-efferentation interferes with the modiolar-pillar gradient of ribbon size[33]. In rodents, the
65 LOC fibers express a variety of neurotransmitters including dopamine (DA), acetylcholine (ACh)
66 and ϒ-amino-butyric acid (GABA) among others (for reviews see ref. 34,35) and was found
67 important for interaural matching[36,37] as well as [1]SGN gain control[38]. The efferent projections of the
68 medial olivocochlear component (MOC) form cholinergic synapses onto outer hair cell (OHC) and
69 suppress their electromotility thereby attenuating cochlear amplification[39-41]. Despite, numerous
70 lesion and pharmacological studies we still lack a comprehensive understanding of how LOC and
71 MOC efferent transmission modulate sound encoding (for reviews see ref. 5,35).

72 Despite earlier structural investigation on cochlear afferent and efferent innervation using light
73 microscopy and conventional electron microscopy[19,42-45], a comprehensive diagram of the neural
74 circuitry in the organ of Corti remains to be established. Here we report the complete reconstruction
75 of a large EM volume acquired from the organ of Corti of the mid-frequency region of the mature
76 mouse cochlea. We employed serial block-face EM (SBEM) imaging[46] which offered the spatial

resolution required for a comprehensive connectomic analysis.

This revealed novel insights into the afferent circuitry such as terminal bifurcation in 12.4 % of the ^{1}SGNs, which results in input of two or more AZs from one or two IHCs. Moreover, we demonstrate MOC innervation of ^{1}SGNs, preferentially of those contacting the pillar IHC side. Further, we show that ^{1}SGNs whose dendrites attract excitation from multiple ribbons also receive efferent modulation at a greater strength, which is achieved by enhanced LOC but weakened MOC innervations. Hence ^{1}SGNs dendrites innervating modiolar and pillar faces of the IHCs receive a fine-tuned MOC and LOC innervation, which likely contributes to differentiating their response properties and, therefore, wide dynamic range sound encoding. These results reveal an unprecedented complexity of the neural circuitry of the organ of Corti. Our analysis provides a morphological framework for interpreting functional studies and offers hypotheses that can now be tested in future experiments and computational efforts.

Results

To perform a comprehensive structural analysis of the mammalian cochlear circuit, we acquired a SBEM dataset from the left cochlea of a 7-week-old wildtype female CBA mouse (**Fig. 1 a** & **b**). The field of scanning was centered on the organ of Corti of the cochlear mid-turn and encompassed 15 IHCs and 45 OHCs. 2500 consecutive image slices were collected, resulting in a 3D-aligned volume of 262 × 194 × 100 μm^3 at 11 × 11 × 40 nm^3 voxel size (**Suppl. video 1** & **2**). Dense reconstruction of the inner spiral bundle (ISB) beneath the 15 IHCs (**Fig. 1 c**) was done by manual annotation using an open-source visualization and annotation software called webKNOSSOS[47]. Despite 40 nm cutting thickness, quantification using a redundant-skeleton consensus procedure (RESCOP)[48] suggests a tracing quality comparable to the published SBEM cortex datasets of 30 nm cutting thickness (**Suppl. Figure 1**). Tracing revealed a total of 234 ^{1}SGNs dendrites, 32 LOC as well as 39 MOC fibers, which contribute 47.2 %, 36.46 %, and 13.05 % to a total circuit path length of 16.97 mm in the ISB region (**Fig. 1 d** & **e**). ^{1}SGNs dendrites were identified as fibers contacting ribbon-type AZs of IHCs (dendrites emanating from ^{1}SGNs) or OHCs (dendrites emanating from ^{2}SGNs crossing the tunnel of Corti). Efferent fibers were defined as LOCs if they exclusively synapsed onto ^{1}SGNs and IHCs and as MOCs if they crossed the tunnel of Corti and also contacted the OHCs. A total of 1517 efferent synapses onto ^{1}SGNs were annotated in the dataset.

Ribbon synapse heterogeneity in IHCs. Volume EM techniques have been recently employed to investigate ribbon synapse morphology in the apical cochlea of C57BL/6 mice at different developmental stages[18]. Our SBEM dataset now provides detailed structural insight into the mature mid-turn and, hence, most sound sensitive region of the cochlea[14,23,42] in the CBA mouse strain.

111 CBA mice are often considered as the gold standard for analyzing normal hearing in mice and do
112 not show the rapid age-related hearing loss of C57BL/6[49]. High spatial resolution and large volume
113 of the dataset allows precise structural quantification of ribbons as well as the postsynaptic ^{1}SGN
114 dendrites (**Fig. 2 a & b**). From 15 reconstructed IHCs, in total 308 ribbons were identified and
115 volume traced by human annotators and ribbon positions were determined in the plane perpendicular
116 to the IHC habenular-cuticular axis (same as described in ref. 33). In agreement with the previous
117 quantification using light microscopy[16,17], a prominent modiolar-pillar size gradient of ribbons was
118 observed (**Fig. 2 c**). On average, ribbons designated to modiolar side of the IHCs (0.0153 ± 0.0055
119 μm^3) are 30 % larger than those to the pillar side (0.0117 ± 0.0049 μm^3, $p < 0.001$).
120 In addition to the heterogeneity of ribbon size within IHC, we found differences in the
121 distributions of ribbon abundance and size between IHCs, even in neighbors (**Fig. 2 d & e**), which
122 has not yet been reported to our knowledge. In some extreme cases, individual IHCs can exclusively
123 contain large or small ribbons, which is unrelated to the characteristic staggering arrangement of
124 IHCs in the cochlea mid-turn[33]. Further, we found in an IHC the mean size of ribbons negatively
125 correlates with the ribbon abundance (**Fig. 2 e**), potentially indicating a conserved amount of cellular
126 ribbon material. Such heterogeneous abundance and average size of ribbons of adjacent IHCs
127 suggests a tuning of their synapses to different fractions of the dynamic sound intensity range.
128
129 **Quantification of afferent and efferent inputs on ^{1}SGN dendrites**. Besides the excitatory input
130 from ribbon-type AZs of IHC, ^{1}SGN dendrites are the primary postsynaptic target of efferent LOC
131 projections. A prior study of the effects of lesioning the LOC projections indicated that innervation
132 by LOCs is required for maintaining the modiolar-pillar ribbon size gradient. Therefore, systematic

133 mapping of efferent innervation profile on ^{1}SGN dendrites postsynaptic to ribbon-type AZs of
134 different morphology and position on IHCs may help to elucidate differential efferent modulation
135 of ^{1}SGNs. Reconstruction of ^{1}SGN dendrites together with their complete afferent and efferent
136 inputs in the ISB region revealed several unexpected findings. First, we found that three
137 morphologically distinct subpopulations of ^{1}SGNs coexist in the mature cochlea (**Fig. 3 a**). Out of
138 total 234 ^{1}SGNs, 170 (72.6 %) are identified as unbranched ^{1}SGNs receiving input from an IHC AZ
139 holding a single ribbon ("single-ribbon variant", **Fig. 3 a1**), 35 (15.0 %) as unbranched ^{1}SGNs but
140 input from multiple ribbons ("unbranched multi-ribbon"), and strikingly 29 (12.4 %) as branched
141 or bifurcated ^{1}SGNs with input from multiple ribbons of one or two IHCs ("branched multi-ribbon",
142 **Fig. 3 a2 & a3** and **Suppl. Figure 2**). Detailed analysis showed that branched ^{1}SGNs more
143 commonly bridged neighboring IHCs (24 out of 29) instead of multiple AZs of single IHC (**Fig. 3 b**).
144 Branched ^{1}SGNs preferentially contacted the modiolar face of the IHCs: 29/29 had at least one
145 modiolar ribbon and 13/29 had only modiolar ribbons, **Fig. 3 b**). As previously reported for the apex
146 of the mouse cochlea[18], AZs with multiple ribbons preferred the modiolar IHC side (20 out of 35)
147 also in our mid-cochlear dataset.

148 Further, we found a varying number of efferent synapses on the unmyelinated segments of
149 ^{1}SGN dendrites, ranging from 0 up to 20 contacts (**Fig. 3 c**). On unbranched and branched multi-
150 ribbon ^{1}SGNs significantly more efferent contacts are formed than on unbranched, single-ribbon
151 ^{1}SGNs (**Fig. 3 d**. 8.82 ± 3.70 for multi-ribbon ^{1}SGNs and 5.70 ± 2.53 for single-ribbon ^{1}SGNs, $p <$
152 0.001). Similarly, stronger efferent innervation was also observed for unbranched, single-ribbon
153 ^{1}SGNs on the IHC modiolar side compared to those on the pillar side (6.37 ± 2.95 for the modiolar
154 ^{1}SGNs and 5.26 ± 2.20 for the pillar ^{1}SGNs, **Fig. 3 d inset,** $p = 0.0073$) but to a lesser extent

155 (**Fig. 3 e**). Considering that large and multi-ribbons are more prevalent on the IHC modiolar side
156 and likely provide greater maximum rates of transmitter release, our data indicates greater strength
157 of efferent modulation of ^{1}SGNs with stronger afferent input. Note that the increased efferent
158 innervation was achieved by more efferent synapses along the ^{1}SGN dendrites in the ISB region
159 rather than in the vicinity of ribbon synapse (**Suppl. Figure 3**).
160
161 **^{1}SGNs are innervated by efferent terminals of both LOC and MOC fibers.** We note that the
162 above analysis of efferent innervation did not separate synapses formed by LOC and MOC fibers.
163 Due to the extent of the reconstruction, it was possible to distinguish MOC fibers from LOC fibers
164 (**Fig. 4 a** to **c**), simply by their characteristic tunnel-crossing (**Fig. 4 d**) and OHC innervation (**Fig.**
165 **4 e**). Unexpectedly, we found that ^{1}SGNs are also frequently contacted by MOC fibers with sparse
166 parallel calibers of variety lengths in the ISB before crossing the tunnel (**Fig. 4 d** to **f**). Compared
167 to LOC synapses (**Fig. 4 c**), MOC terminals on ^{1}SGN dendrites showed larger bouton size but
168 sparser vesicle content (**Fig. 4 f**). Extended structural quantification of all 39 MOC and 32 LOC
169 fibers revealed that MOC fibers form fewer efferent synapses in the ISB region (**Fig. 4 e**) and
170 preferentially innervate ^{1}SGN dendrites originating from the pillar IHC side (**Fig. 4 f**). This is
171 consistent with the observation that MOC-innervated ^{1}SGNs have small ribbon size (**Fig. 4 g**) and
172 receive weaker efferent innervation (**Fig. 4 h**). In conclusion, this data suggests a hitherto unreported
173 function of MOC fibers in modulating ^{1}SGNs, particularly those contacting the IHC pillar side.
174 Together with the preference of LOC fibers to innervate modiolar ^{1}SGNs, the data indicates
175 differential modulation of ^{1}SGNs by projections from medial and lateral subdivisions of the superior
176 olivary complex.

Spatial organization of efferent innervation on ^{1}SGNs. As described above, both LOC and MOC innervation coexists on individual ^{1}SGN dendrites and their presynaptic terminals have distinct appearances (**Fig. 4 c** & **f**). By these criteria, we identified 1175 putative LOC and 342 putative MOC terminals out of the total of 1517 efferent contacts on ^{1}SGN dendrites. Consistent with the reported innervation specificity of LOC and MOC projections, the dendrite-based analysis of efferent input indicates that both modiolar and multi-ribbon ^{1}SGNs receive strong LOC innervations (**Fig. 5 a**) but weak MOC innervations (**Fig. 5 b**). Note that MOC synapses avoid more than half of modiolar and multi-ribbon ^{1}SGNs (**Fig. 4 f**) and were preferentially found on the pillar ^{1}SGNs that featured few LOC synapses. As a direct consequence, the efferent composition showed ^{1}SGN-subdivision-specific heterogeneity: predominantly LOC inputs on modiolar and multi-ribbon ^{1}SGNs; mixed inputs on pillar ^{1}SGNs (**Fig. 5 c**). Finally, we found a segregation of MOC and LOC innervation sites on ^{1}SGN dendrites with LOC terminals being more proximal to the ribbon synapses and MOC terminals located exclusively near of hemi-node (**Fig. 5 d**). The spatial distribution of efferent terminals within the ISB (**Fig. 5 e**) as well as the efferent fiber trajectories (**Fig. 5 f**) show the spatial segregation of the MOC and LOC projections, which might instruct their preferred ^{1}SGN innervation.

Discussion

In the last decade, high throughput volume EM techniques have rendered dense reconstruction of large-scale mammalian neural circuits realistic within reasonable time and costs[50,51]. SBEM and FIB-SEM offer several advantages over other volume EM techniques based on thin slice collection, including less image distortion and fully automated acquisition cycle [51,52]. Despite less z-resolution, in the end we chose SBEM instead of FIB-SEM in order to cover a larger volume for a more comprehensive circuit level analysis in the organ of Corti. Additional iterations of system optimization were made to overcome technical issues like charging artefacts and limited cutting thickness. Finally, by combining optimized sample preparation procedure to increase tissue conductivity, implementing focal charge compensation to minimize charging from pure resin area, and cutting along the direction of efferent calibers to improve the traceability at 40 nm z-resolution, we managed to acquire a dataset that allowed dense circuit reconstruction in the mature cochlea. Moreover, the established workflow can now be applied to healthy and diseased cochlear tissues at different animal ages, for instance in animal models of genetic, noise- or age-related hearing loss. The volume EM analysis of this study provided both rigorous testing of important concepts on cochlear circuitry as well as novel observations that allowed us to generate new hypotheses.

Afferent connectivity of ^{1}SGNs: graded synaptic strength and postsynaptic information mixing

The prevailing view on the afferent connectivity of ^{1}SGNs in the mature mammalian cochlea is the mono-synaptic contact with a single-ribbon. One of the striking findings of the present study is the existence of a considerable number of branched ^{1}SGNs (12.4 %) characterized by a bifurcation of

217 the ^{1}SGN dendrite forming multiple synaptic contacts with one or two IHC(s) (**Fig. 3 a** and **Suppl.**
218 **Figure 2**). The branched, multi-ribbon ^{1}SGNs further diversify the afferent connectivity with regard
219 to presynaptic IHCs, site of contact as well as ribbon morphology. It is tempting to speculate that
220 instead of basing the mammalian auditory afferent pathway exclusively on single-ribbon connection,
221 adding those variations may extend the dynamic range of sound coding. Peripheral branching of
222 afferent neurons is highly prevalent found in the hearing organs of birds and lower vertebrates[53,54].

223 So far, the presence of multiple ribbons at a single AZ was considered the exception to the rule
224 and, if encountered, to occur at modiolar AZs[12,15,18,19]. Here, we found that about 15 % afferent
225 contacts contain more than one ribbon in the middle turn of the mouse cochlea (**Fig. 3 a**). We
226 demonstrate the modiolar-pillar size gradient of ribbon size and abundance for IHC AZs at the level
227 of electron microscopy for a large sample of 308 synapses (**Fig. 2 d**). This corroborates previous
228 light microscopy[16,17] and electron microscopy[15,19,55] studies. Together with the notion of the
229 preference of low spontaneous rate, high threshold ^{1}SGNs for modiolar AZs this begs the questions
230 how presynaptic strength can relate to weaker sound responses. One candidate mechanism to
231 explain this apparent conundrum is the more depolarized activation range of the Ca^{2+} influx at the
232 modiolar AZs[17]. We note that recently, an instructive role of Pou4f1-expressing, presumably low
233 spontaneous rate, high threshold ^{1}SGNs on AZ size has been indicated[56]. Moreover, a completely
234 different means of regulation resulting from planar polarity signaling was implied in setting up the
235 modiolar-pillar gradient of AZ size[55]. Our present study suggests that stronger efferent modulation
236 of ^{1}SGNs facing multi-ribbon AZs also contributes (see next section).

237 In the reconstructed volume 15 IHCs were arranged in a partially staggered fashion that is
238 prevalent in the cochlea mid-turn[33]. However, the influence of the staggered IHC arrangement on

239 ribbon size seems minor if present at all (**Fig. 2 d & e**): IHCs closer to the pillar side tended to have
240 smaller ribbons on average than those closer to the modiolus. Nevertheless, the notable negative
241 correlation between the size and abundance of ribbons in IHCs (**Fig. 2 e**) suggests an endogenous
242 control of total supply of ribbon material.
243

244 **Balancing the strength of afferent and efferent inputs into ^{1}SGNs**

245 A key result of the present study is the observation that stronger afferent input by multi-ribbon AZs
246 and/or multiple synapses is accompanied by stronger efferent innervation (**Fig. 3 d & e**). Previous
247 studies showed a shifted acoustic sensitivity of ^{1}SGNs to higher sound pressure levels during
248 efferent activation[57,58], resetting the dynamic range. Matched enhancement of afferent (ribbon) and
249 efferent strength on ^{1}SGNs may allow a tuning of the dynamic range on demands, which provides
250 a possible explanation for discrimination of small intensity changes as well as sound source
251 localization in a background-adaptive fashion. Moreover, surgical de-efferentation of the adult
252 mouse cochlea was shown to attenuate the modiolar-pillar gradient of ribbon size, suggesting a key
253 role for the efferent system in maintaining functional heterogeneity of the afferent synapses[33]. Hence,
254 efferent innervation might contribute to shaping neural response diversity underlying wide dynamic
255 range coding by modulating ^{1}SGNs as well as by instructing the synaptic properties in a position-
256 dependent manner.

257 To our knowledge, this comprehensive EM circuit analysis of a large cochlear volume, for the
258 first time found MOC fibers to make considerable amounts of synaptic contacts with ^{1}SGN dendrites
259 just before leaving the ISB region towards OHCs (**Fig. 4 d**). It seems to be a general feature of MOC
260 innervation, because this kind of connections was found in 37 out of 39 annotated MOC fibers

(**Fig. 4 e**), indicating a novel function of MOC modulation in ^{1}SGN activities beyond its well-identified suppressive effect on OHC motility[39-41].

It is remains to be studied whether MOC fibers employ acetylcholine as single neurotransmitter in terminals on both ^{1}SGN dendrites and OHCs. If that is the case, based on the observation of acetylcholine injection experiment[59] one might expect a simultaneous elevation of both spontaneous and evoked firing rate of ^{1}SGNs in addition to the classic MOC-mediated suppression of cochlear amplification. This way, MOC modulation might contribute to the high spontaneous firing rate of ^{1}SGNs contacting the pillar IHC side (**Fig. 5 b**). MOC terminals are found restricted to the proximity of heminode (**Fig. 5 d**), which may overlap with the innervation site of putative inhibitory dopaminergic LOC fibers[60].

This study presents a comprehensive circuit map with quantification that enriches our insight into the structure underlying auditory signal processing. Besides novel insight into normal cochlear structure, the result of circuit analysis serves as a baseline for future structural investigations, including noise-induced synaptopathy[61], aging-related structural alteration[62,63] and putative tinnitus-related synaptic plasticity changes[64].

Acknowledgements

We thank Prof. M.Lei (SHIPM) for discussion and comments on the manuscript; thank Prof. M.Helmstaedter (MPI-BR) for support in the initial phase of the project; thank R.Redman, P.Bastians from Zeiss (APAC) for technical advice; thank Y.Lu, D.Li, J.Pan, J.Lu, H.Liu, B.Feng, Z.Jiang, C.Jin, L.Zhou, X.Yu, W.Wang, G.Li and Z.Chen for the tracing work. This study was supported by The Program for Professor of Special Appointment (Eastern Scholar) at Shanghai

Institutions of Higher Learning (QD2018015 to Y.H.), the National Natural Science Foundation of China (81800901 to Y.H. and 81730028 to H.W.), the National Basic Research Development Program of China (SQ2017YFSF080012 to H.W.) and Shanghai Key Laboratory of Translational Medicine on Ear and Nose Diseases (14DZ2260300). Work by T.M. was supported by the German Research Foundation through the Leibniz program and the MBExC.

Declarations of interest

The authors have declared that no conflicts of interest exist.

Author contributions

Y.H., H.W. and T.M. designed and supervised the study. Y.H., X.D., H.H.W., F.W. performed the SBEM experiment, Y.H. and H.H.W. analyzed the data. X.D., G.Y. assisted with the data analysis. Y.H., and T.M., wrote the manuscript with the help of all authors.

Figure legends

Figure 1 SBEM imaging and dense reconstruction of mouse organ of Corti. (a) Location of the SBEM dataset (green box) in the resin-embedded cochlea. **(b)** Dimension of the dataset. Red box: virtual cross-section at the position as indicated in (a, left). **(c)** High-resolution example image of neurites beneath IHCs and a representative ^{1}SGN terminal was indicated by asterisk (green). Sale bar 2 μm**. (d)** Reconstruction of all 322 neurites in the dataset. Left: skeletons of all ^{1}SGNs (green) and one representative ^{2}SGN dendrite (grey). Right: skeletons of all LOC fibers (blue) and MOC fibers (magenta) with main trunks extending into habenular perforate and tunnel-crossing fibers

305 towards OHC region. Small grey spheres represent OHCs and large dark spheres represent IHCs.
306 Scale bar 20 μm. **(d, e)** Quantification of circuit components. All 234 ^{1}SGNs (green), 32 LOC fibers
307 (blue) and 39 MOC fibers (magenta) contribute 47.2 % (8.01 mm), 36.46 % (6.19 mm) and 13.05 %
308 (2.21 mm) of circuit path length (total: 16.97 mm) in the ISB region, respectively.
309
310 **Figure 2 Quantification of synaptic ribbons in the IHCs. (a)** Consecutive slices showing a
311 representative ribbon synapse (red box) and the postsynaptic ^{1}SGN terminal (green) co-innervated
312 by an efferent terminal (blue). Scale bar 1 μm. **(b)** Volume reconstruction of an example IHC with
313 all ribbon synapses (red) and ^{1}SGNs (green), and a representative LOC fiber (blue). Scale bar 5 μm.
314 IHC location was indicated in Suppl. Figure 1. **(c)** Boxplot of measured ribbon sizes. All 308
315 identified ribbons were classified as two classes according to their locations (pillar or modiolar side)
316 in the IHCs. Exceptions are 12 cases for which ribbons were located at the bottom of IHC. Note that
317 ribbons on the IHC pillar side (black dots, 0.0117 ± 0.0049 μm^3) are significantly smaller than their
318 counterparts on the modiolar side (grey dots, 0.0153 ± 0.0055 μm^3). (Two-sample t-test, ***$p <$
319 0.001). **(d)** Cumulative probability distribution of ribbon sizes from all 15 IHCs (red), as well as
320 individual IHCs proximal (black, n = 7) and distal (grey, n = 8) to the modiolus. Note the remarkable
321 cell-to-cell variability between IHCs. **(e)** Negative correlation between number and mean size of
322 ribbons in individual IHCs. (Linear fit: adjusted-$R^2 = 0.67$).
323
324 **Figure 3 Quantification of ribbon and efferent inputs on ^{1}SGN dendrites (a)** Volume
325 reconstruction of three distinct ^{1}SGN classes characterized by single-ribbon (unbranched ^{1}SGN,
326 left), multi-ribbon (unbranched ^{1}SGN, middle), and bifurcation (branched ^{1}SGN, right). They

327 constitute 72.6 %, 15.0 %, and 12.4 % of all reconstructed ^{1}SGN dendrites. Inset: (**a1-a4**) cross-
328 sections through synaptic structures indicated in (a) with arrows. Single-ribbon contact (**a1**), dual-
329 ribbon contact (**a2**), ribbons on bifurcated ^{1}SGN (**a2** & **a3**), and an example efferent synapse onto
330 ^{1}SGN dendritic shaft (**a4**). **(b)** Ribbon classification of multi-ribbon and branched ^{1}SGNs. Left: 57 %
331 (20 out of 35) multi-ribbon ^{1}SGNs receive inputs from exclusive modiolar ribbons (Mod.), 34 %
332 (12) from pillar ribbons (Pillar) and 9 % (3) from ribbons at IHC bottom (Mixed). Middle and right:
333 branched ^{1}SGNs are postsynaptic to single or multiple IHCs with both modiolar and pillar ribbons.
334 34 % (10 out of 29) branched ^{1}SGNs which are onto multiple IHCs have exclusively modiolar
335 ribbons (Mod.) and 66 % (19) have both modiolar and pillar ribbons (Mixed), while that number is
336 80 % (4 out of 5, Mid.) and 20 % (1, Mixed) for bifurcated ^{1}SGNs on single IHC**. (c)** Display of
337 full-length unmyelinated ^{1}SGN dendrites (green) with presynaptic ribbons (red) and efferent
338 synapses (OC inputs, blue). Scale bar 20 μm. **(d)** Histograms of efferent synapse number on ^{1}SGN
339 dendrites grouped according to ribbon structures. Multi-ribbon ^{1}SGNs (red, n = 63) has the trend of
340 receiving more efferent synapses than single-ribbon ^{1}SGN (black, n = 172), while the difference in
341 efferent synapse number between ^{1}SGNs postsynaptic to single modiolar ribbon (grey) and those to
342 single pillar ribbon (black) is less prominent. **(e)** Quantification of the result from (d). On average
343 5.70 ± 2.53 and 8.82 ± 3.70 efferent synapses were found innervating an ^{1}SGN with single- (black
344 filled) and multi-ribbon (red filled). For ^{1}SGNs with single-ribbon, efferent synapses innervating
345 pillar ^{1}SGNs (black open) and modiolar ^{1}SGNs (grey open) were 5.25 ± 2.19 and 6.47 ± 2.81,
346 respectively. Two-sample t-tests suggest significant difference between single and multi-ribbon
347 ^{1}SGNs (***$p < 0.001$) as well as between ^{1}SGNs with single pillar and modiolar ribbon (**$p =$
348 0.0028).

Figure 4 Innervation specificity of OC fibers. (a) Display of a representative LOC fiber (blue) with all 25 innervated ^{1}SGNs (green) in the dataset. Scale bar 20 µm. **(b-c)** High-resolution example image of presynaptic LOC synapse onto an IHC (blue arrow, open) and on ^{1}SGN dendrite (blue arrow, filled). Scale bar 1 µm. **(d)** Display of a representative MOC fiber (magenta) with all seven innervated ^{1}SGNs (green) in the dataset. Scale bar 20 µm. **(e & f)** High-resolution example image of presynaptic MOC synapse onto an OHC (magenta arrow, open) and on ^{1}SGN dendrite (magenta arrows, filled). Scale bar 1 µm. **(g)** Boxplot showing the comparison between output synapse number of individual MOC fibers (magenta) and LOC fibers (blue). **(h)** Innervation selectivity of MOC fibers (magenta) and LOC fibers (blue) on ^{1}SGNs postsynaptic to pillar and modiolar ribbon. For selectivity index $S = (\#^{1}SGN_{Mod.} - \#^{1}SGN_{Pillar}) / (\#\,^{1}SGN_{Mod.} + \#^{1}SGN_{Pillar})$. Note that 30 out of 39 MOC fibers innervate exclusively pillar ^{1}SGNs. **(i)** Boxplot showing mean ribbon size of MOC-innervated ^{1}SGNs (magenta) compared to that of LOC-innervated ^{1}SGNs (blue). **(j)** Cumulative probability distribution of efferent synapse numbers on individual MOC-innervated ^{1}SGNs (magenta) compared to that of LOC-innervated ^{1}SGNs (blue). (For g to i, two-sample t-test, ***$p < 0.001$; for j, two-sample Kolmogorov-Smirnov test, ***$p < 0.001$).

Figure 5 Dendritic sorting of OC innervation on ^{1}SGN dendrites (a) Cumulative probability distribution of LOC synapse numbers on individual ^{1}SGNs with single-pillar ribbon (light blue, thin line), single-modiolar ribbon (dark blue, thin line), and multi-ribbons (blue, thick line). **(b)** Similar to (a), cumulative probability distribution of MOC synapse number on individual ^{1}SGNs with single-pillar ribbon (light magenta, thin line), single-modiolar ribbon (dark magenta, thin line), and

371 multi-ribbons (magenta, thick line). Note that MOC synapse is absent from over 50 % ^{1}SGNs with
372 modular ribbon or multi-ribbons (magenta). **(c)** Counts of ^{1}SGNs with different percentage of LOC
373 synapse in total OC synapses with respect to single-pillar ribbon (small black dots), single-modiolar
374 ribbon (small grey dots), as well as multi-ribbons (large grey dots). **(d)** Measurement of dendritic
375 path lengths from MOC synapse (magenta) or LOC synapse (blue) to the heminode of ^{1}SGN
376 dendrite. **(e & f)** 3D-illustration showing spatial segregation of LOC synapses (blue) from MOC
377 synapses (magenta) (e), as well as traced trajectories of LOC (blue) from those of MOC fibers
378 (magenta) (f). (For a, b and d two-sample Kolmogorov-Smirnov test, ***$p < 0.001$).
379
380 **Supplementary Figure 1.** Quantification of tracing accuracy (**a**) 7-fold skeletonization of the ^{1}SGN
381 dendrites and an efferent axon traced by trained non-experts in the dataset. For ^{1}SGN dendrites, all
382 tracing started from the postsynaptic terminal to a given ribbon synapse till the locations of
383 myelination. Grey spheres represent the nuclei of IHCs which are arranged in a staggered manner.
384 Scale bar 5 μm. (**b-d**) RESCOP analysis of traceability: histogram of edge votes (**b**), estimated edge-
385 detection probability $p(p_e)$ distribution for all traced neurites (**c**), and prediction of tracing accuracy
386 as a function of annotation redundancy (**d**).
387
388 **Supplementary Figure 2.** Ten skeleton examples of bifurcated ^{1}SGN dendrites. Red dots represent
389 ribbon synapses and blue dots represent efferent OC synapses. Scale bar 10 μm.
390
391 **Supplementary Figure 3.** Similar efferent innervation on afferent terminals on both IHC sides. **(a)**
392 an example image of ^{1}SGN terminal (green). Efferent synapse with physical contact was marked by
393 red asterisk and those within a 4-μm-sized box (white) but without physical contact by white

394 asterisks. Scale bar 1 μm. **(b)** Boxplot of efferent synapse number on [1]SGN terminals on IHC
395 modiolar (left) and pillar side (right). Statistical significance was not found. (Two-sample t test: p =
396 0.0837).
397

398 **Material and Methods**

399 **Animals.** CBA/Ca mice were purchased from Sino-British SIPPR/BK Lab.Animal Ltd (Shanghai,
400 China). This study is conduct at Shanghai Institute of Precision Medicine and Ear Institute of
401 Shanghai Ninth People's Hospital. All procedures were reviewed and approved by the Institutional
402 Authority for Laboratory Animal Care of the hospital (SH9H-2019-A387-1).
403

404 **Whole cochlea EM preparation.** Animal were anesthetized through intraperitoneal injection of
405 hydrate chloride (500 mg/kg) and temporal bones were removed after decapitation. The cochleae
406 were fixed by perfusion through the round window with ice-cold fixative mixture containing 0.08M
407 cacodylate (pH 7.4), 2% freshly-made paraformaldehyde (Sigma), 2.5% glutaraldehyde (Sigma),
408 and then immersion-fixed for 5 hours, followed by 4-hour decalcification in the same fixative with
409 addition of 5% EDTA (ethylenediaminetetraacetic acid, Sigma-Aldrich).
410 The *en bloc* EM staining was performed following the previously published protocol[65] with
411 modifications. In brief, the decalcified cochleae were washed twice in 0.15M cacodylate (pH 7.4)
412 for 30 min and sequentially immersed in 2% OsO_4 (Ted Pella), 2.5% ferrocyanide (Sigma) and again
413 2% OsO_4 at room temperature for 2, 2 and 1.5 hours without intermediate washing step. All staining
414 solutions were buffered with 0.15M cacodylate (pH 7.4). After being washed twice in nanopore
415 filtered water for 30 min each, the cochleae were incubated at room temperature in filtered

416 thiocarbonhydrazide (saturated aqueous solution, Sigma) for 1 hour, unbuffered OsO_4 aqueous
417 solution for 2 hours and in lead aspartate solution (0.03M, pH 5.0 adjusted by KOH, EMS) at 50C°
418 for 2 hours. Between steps, double rinses in nanopore filtered water for 30 min each.
419 For embedding, the cochleae were first dehydrated through a graded acetone (50%, 75%, 90%, 30
420 min each, all cooled at 4C°) into pure acetone (3×100%, 30 min at room temperature), followed by
421 sequential infiltration with 1:1 and 1:2 mixtures of acetone and Spurr's resin monomer (4.1g ERL
422 4221, 0.95g DER 736, 5.9g NSA and 1% DMAE; Sigma-Aldrich) at room temperature for 6 hours
423 each on a rotator. Infiltrated cochleae were then incubated in pure resin overnight before being
424 placed in embedding molds (Polyscience, Germany) and incubated in a pre-warmed oven (70C°)
425 for 72 hours.
426
427 **SBEM imaging of cochlea.** Embedded samples were trimmed to a block-face of ~ 800 × 800 μm^2
428 and imaged using a field-emission scanning EM (Gemini300, Zeiss) equipped with an in-chamber
429 ultramicrotome (3ViewXP, Gatan) and back-scattered electron detector (Onpont, Gatan). Serial
430 images were acquired in single tile mode (20,000 × 15,000 pixels) of 11 nm pixel size and nominal
431 cutting thickness of 40 nm; incident beam energy 2 keV; dwell time 1 µs. 2500 slices were collected.
432 Focal charge compensation[66] was set to 100% with a high vacuum chamber pressure of ~2.8 ×
433 10^{-3} mbar. The dataset was aligned using self-written MATLAB script based on cross-correlation
434 maximum between consecutive slices. Then the aligned dataset was split into cubes (128 × 128 ×
435 128 voxels) for viewing and neurite-tracing in a browser-based annotation tool called
436 webKNOSSOS[47].
437

Neurite reconstruction and traceability test. Seed points were generated from 17 annotated afferent and one efferent terminal beneath an IHC at central region of the dataset. These coordinates were delivered to annotators as start points for neurite-tracing in all directions within the data volume. This yielded 19 × 7 = 133 skeletons with a total length of 7.185 mm, which were further analyzed using the RESCOP[48] routine as described previously[65]. In brief, each set of seven redundant skeletons was compared computing the number of 'pro' votes and total votes for each edge in each skeleton-tracing. This resulted in a vote histogram that was corrected for the redundancy of each tracing, yielding the measured vote histogram. Next, the underlying prior of edge probability $p(p_e)$ was determined by fitting the vote histogram under the simplifying assumption that tracing decisions were independent between tracers and locations. Then, the predicted mean error-free path length as a function of the number of tracings per seed point ('tracing redundancy') was computed from the fitted prior $p(p_e)$ for the setting of annotators reconstructing a neurite.

Ribbon size measurement and synapse counting. The ribbon size was measured by counting voxels which belonged to individual ribbon structures via volume-tracing tool in the webKNOSSOS. Efferent synapse annotation was done by three independent annotators on traced skeletons and the result was proof-read by inspecting of a 4th annotator at annotated locations. All data analysis including statistic tests were conduct using self-written script and build-in functions in MATLAB (Mathworks).

Additional information

Suppl. Video 1: Down-sampled cochlea SBEM data with alignment (scale bar 10 µm)

Suppl. Video 2: High resolution cochlea SBEM data in the ISB region (scale bar 2 µm)

References

1 Moser, T., Grabner, C. P. & Schmitz, F. Sensory Processing at Ribbon Synapses in the Retina and the Cochlea. *Physiol Rev* **100**, 103-144, doi:10.1152/physrev.00026.2018 (2020).

2 Fettiplace, R. Hair Cell Transduction, Tuning, and Synaptic Transmission in the Mammalian Cochlea. *Compr Physiol* **7**, 1197-1227, doi:10.1002/cphy.c160049 (2017).

3 Huet, A. *et al.* Sound Coding in the Auditory Nerve: From Single Fiber Activity to Cochlear Mass Potentials in Gerbils. *Neuroscience* **407**, 83-92, doi:10.1016/j.neuroscience.2018.10.010 (2019).

4 Reijntjes, D. O. J. & Pyott, S. J. The afferent signaling complex: Regulation of type I spiral ganglion neuron responses in the auditory periphery. *Hear Res* **336**, 1-16, doi:10.1016/j.heares.2016.03.011 (2016).

5 Fuchs, P. A. & Lauer, A. M. Efferent Inhibition of the Cochlea. *Cold Spring Harb Perspect Med* **9**, doi:10.1101/cshperspect.a033530 (2019).

6 Liberman, M. C. Single-neuron labeling in the cat auditory nerve. *Science* **216**, 1239-1241, doi:10.1126/science.7079757 (1982).

7 Kiang, N. Y. S. *Discharge patterns of single fibers in the cat's auditory nerve. With the assistance of Takeshi Watanabe [et al.].* (M. I. T. Press, 1965).

8 Safieddine, S., El-Amraoui, A. & Petit, C. The auditory hair cell ribbon synapse: from assembly to function. *Annu Rev Neurosci* **35**, 509-528, doi:10.1146/annurev-neuro-061010-113705 (2012).

9 Khimich, D. *et al.* Hair cell synaptic ribbons are essential for synchronous auditory signalling. *Nature* **434**, 889-894, doi:10.1038/nature03418 (2005).

10 Frank, T. *et al.* Bassoon and the synaptic ribbon organize Ca(2)+ channels and vesicles to add release sites and promote refilling. *Neuron* **68**, 724-738, doi:10.1016/j.neuron.2010.10.027 (2010).

11 Becker, L. *et al.* The presynaptic ribbon maintains vesicle populations at the hair cell afferent fiber synapse. *Elife* **7**, doi:10.7554/eLife.30241 (2018).

12 Jean, P. *et al.* The synaptic ribbon is critical for sound encoding at high rates and with temporal precision. *Elife* **7**, doi:ARTN e29275
10.7554/eLife.29275 (2018).

13 Frank, T., Khimich, D., Neef, A. & Moser, T. Mechanisms contributing to synaptic Ca2+ signals and their heterogeneity in hair cells. *Proc Natl Acad Sci U S A* **106**, 4483-4488, doi:10.1073/pnas.0813213106 (2009).

14 Meyer, A. C. *et al.* Tuning of synapse number, structure and function in the cochlea. *Nat Neurosci* **12**, 444-453, doi:10.1038/nn.2293 (2009).

15 Merchan-Perez, A. & Liberman, M. C. Ultrastructural differences among afferent synapses on cochlear hair cells: correlations with spontaneous discharge rate. *J Comp Neurol* **371**,

208-221, doi:10.1002/(SICI)1096-9861(19960722)371:2<208::AID-CNE2>3.0.CO;2-6 (1996).

16 Liberman, L. D., Wang, H. & Liberman, M. C. Opposing gradients of ribbon size and AMPA receptor expression underlie sensitivity differences among cochlear-nerve/hair-cell synapses. *J Neurosci* **31**, 801-808, doi:10.1523/JNEUROSCI.3389-10.2011 (2011).

17 Ohn, T. L. *et al.* Hair cells use active zones with different voltage dependence of Ca2+ influx to decompose sounds into complementary neural codes. *Proc Natl Acad Sci U S A* **113**, E4716-4725, doi:10.1073/pnas.1605737113 (2016).

18 Michanski, S. *et al.* Mapping developmental maturation of inner hair cell ribbon synapses in the apical mouse cochlea. *Proc Natl Acad Sci U S A* **116**, 6415-6424, doi:10.1073/pnas.1812029116 (2019).

19 Kantardzhieva, A., Liberman, M. C. & Sewell, W. F. Quantitative analysis of ribbons, vesicles, and cisterns at the cat inner hair cell synapse: correlations with spontaneous rate. *J Comp Neurol* **521**, 3260-3271, doi:10.1002/cne.23345 (2013).

20 Neef, J. *et al.* Quantitative optical nanophysiology of Ca(2+) signaling at inner hair cell active zones. *Nat Commun* **9**, 290, doi:10.1038/s41467-017-02612-y (2018).

21 Liberman, M. C. Auditory-nerve response from cats raised in a low-noise chamber. *J Acoust Soc Am* **63**, 442-455, doi:10.1121/1.381736 (1978).

22 Wu, J. S., Young, E. D. & Glowatzki, E. Maturation of Spontaneous Firing Properties after Hearing Onset in Rat Auditory Nerve Fibers: Spontaneous Rates, Refractoriness, and Interfiber Correlations. *J Neurosci* **36**, 10584-10597, doi:10.1523/JNEUROSCI.1187-16.2016 (2016).

23 Taberner, A. M. & Liberman, M. C. Response properties of single auditory nerve fibers in the mouse. *J Neurophysiol* **93**, 557-569, doi:10.1152/jn.00574.2004 (2005).

24 Winter, I. M., Robertson, D. & Yates, G. K. Diversity of characteristic frequency rate-intensity functions in guinea pig auditory nerve fibres. *Hear Res* **45**, 191-202, doi:10.1016/0378-5955(90)90120-e (1990).

25 Shrestha, B. R. *et al.* Sensory Neuron Diversity in the Inner Ear Is Shaped by Activity. *Cell* **174**, 1229-1246 e1217, doi:10.1016/j.cell.2018.07.007 (2018).

26 Sun, S. *et al.* Hair Cell Mechanotransduction Regulates Spontaneous Activity and Spiral Ganglion Subtype Specification in the Auditory System. *Cell* **174**, 1247-1263 e1215, doi:10.1016/j.cell.2018.07.008 (2018).

27 Petitpre, C. *et al.* Neuronal heterogeneity and stereotyped connectivity in the auditory afferent system. *Nat Commun* **9**, 3691, doi:10.1038/s41467-018-06033-3 (2018).

28 Meyer, A. C. & Moser, T. Structure and function of cochlear afferent innervation. *Curr Opin Otolaryngol Head Neck Surg* **18**, 441-446, doi:10.1097/MOO.0b013e32833e0586 (2010).

29 Heil, P. & Peterson, A. J. Basic response properties of auditory nerve fibers: a review. *Cell Tissue Res* **361**, 129-158, doi:10.1007/s00441-015-2177-9 (2015).

30 Pangrsic, T., Singer, J. H. & Koschak, A. Voltage-Gated Calcium Channels: Key Players in Sensory Coding in the Retina and the Inner Ear. *Physiol Rev* **98**, 2063-2096, doi:10.1152/physrev.00030.2017 (2018).

31 Warr, W. B. & Guinan, J. J., Jr. Efferent innervation of the organ of corti: two separate systems. *Brain Res* **173**, 152-155, doi:10.1016/0006-8993(79)91104-1 (1979).

32 Nouvian, R., Eybalin, M. & Puel, J. L. Cochlear efferents in developing adult and

544 pathological conditions. *Cell Tissue Res* **361**, 301-309, doi:10.1007/s00441-015-2158-z
545 (2015).
546 33 Yin, Y., Liberman, L. D., Maison, S. F. & Liberman, M. C. Olivocochlear innervation maintains
547 the normal modiolar-pillar and habenular-cuticular gradients in cochlear synaptic
548 morphology. *J Assoc Res Otolaryngol* **15**, 571-583, doi:10.1007/s10162-014-0462-z
549 (2014).
550 34 Eybalin, M. Neurotransmitters and neuromodulators of the mammalian cochlea. *Physiol*
551 *Rev* **73**, 309-373, doi:10.1152/physrev.1993.73.2.309 (1993).
552 35 Ruel, J. *et al.* Physiology, pharmacology and plasticity at the inner hair cell synaptic
553 complex. *Hear Res* **227**, 19-27, doi:10.1016/j.heares.2006.08.017 (2007).
554 36 Darrow, K. N., Maison, S. F. & Liberman, M. C. Cochlear efferent feedback balances
555 interaural sensitivity. *Nat Neurosci* **9**, 1474-1476, doi:10.1038/nn1807 (2006).
556 37 Irving, S., Moore, D. R., Liberman, M. C. & Sumner, C. J. Olivocochlear efferent control in
557 sound localization and experience-dependent learning. *J Neurosci* **31**, 2493-2501,
558 doi:10.1523/JNEUROSCI.2679-10.2011 (2011).
559 38 Eybalin, M., Caicedo, A., Renard, N., Ruel, J. & Puel, J. L. Transient Ca2+-permeable AMPA
560 receptors in postnatal rat primary auditory neurons. *Eur J Neurosci* **20**, 2981-2989,
561 doi:10.1111/j.1460-9568.2004.03772.x (2004).
562 39 Evans, M. G., Lagostena, L., Darbon, P. & Mammano, F. Cholinergic control of membrane
563 conductance and intracellular free Ca2+ in outer hair cells of the guinea pig cochlea. *Cell*
564 *Calcium* **28**, 195-203, doi:10.1054/ceca.2000.0145 (2000).
565 40 Dallos, P. *et al.* Acetylcholine, outer hair cell electromotility, and the cochlear amplifier. *J*
566 *Neurosci* **17**, 2212-2226 (1997).
567 41 Blanchet, C., Erostegui, C., Sugasawa, M. & Dulon, D. Acetylcholine-induced potassium
568 current of guinea pig outer hair cells: its dependence on a calcium influx through
569 nicotinic-like receptors. *J Neurosci* **16**, 2574-2584 (1996).
570 42 Ehret, G. & Frankenreiter, M. Quantitative analysis of cochlear structures in the house
571 mouse in relation to mechanisms of acoustical information processing. *Journal of*
572 *Comparative Physiology* **122**, 66-85, doi:https://doi.org/10.1007/BF00611249 (1977).
573 43 Maison, S. F., Adams, J. C. & Liberman, M. C. Olivocochlear innervation in the mouse:
574 immunocytochemical maps, crossed versus uncrossed contributions, and transmitter
575 colocalization. *J Comp Neurol* **455**, 406-416, doi:10.1002/cne.10490 (2003).
576 44 Fuchs, P. A., Lehar, M. & Hiel, H. Ultrastructure of cisternal synapses on outer hair cells of
577 the mouse cochlea. *J Comp Neurol* **522**, 717-729, doi:10.1002/cne.23478 (2014).
578 45 Thiers, F. A., Nadol, J. B., Jr. & Liberman, M. C. Reciprocal synapses between outer hair
579 cells and their afferent terminals: evidence for a local neural network in the mammalian
580 cochlea. *J Assoc Res Otolaryngol* **9**, 477-489, doi:10.1007/s10162-008-0135-x (2008).
581 46 Denk, W. & Horstmann, H. Serial block-face scanning electron microscopy to reconstruct
582 three-dimensional tissue nanostructure. *PLoS Biol* **2**, e329,
583 doi:10.1371/journal.pbio.0020329 (2004).
584 47 Boergens, K. M. *et al.* webKnossos: efficient online 3D data annotation for connectomics.
585 *Nat Methods* **14**, 691-694, doi:10.1038/nmeth.4331 (2017).
586 48 Helmstaedter, M., Briggman, K. L. & Denk, W. High-accuracy neurite reconstruction for
587 high-throughput neuroanatomy. *Nat Neurosci* **14**, 1081-1088, doi:10.1038/nn.2868

(2011).
49 Willott, J. F. *Handbook of mouse auditory research : from behavior to molecular biology*. (CRC Press, 2001).
50 Helmstaedter, M. Cellular-resolution connectomics: challenges of dense neural circuit reconstruction. *Nat Methods* **10**, 501-507, doi:10.1038/nmeth.2476 (2013).
51 Kornfeld, J. & Denk, W. Progress and remaining challenges in high-throughput volume electron microscopy. *Curr Opin Neurobiol* **50**, 261-267, doi:10.1016/j.conb.2018.04.030 (2018).
52 Briggman, K. L. & Bock, D. D. Volume electron microscopy for neuronal circuit reconstruction. *Curr Opin Neurobiol* **22**, 154-161, doi:10.1016/j.conb.2011.10.022 (2012).
53 Fischer, F. P. Quantitative analysis of the innervation of the chicken basilar papilla. *Hear Res* **61**, 167-178, doi:10.1016/0378-5955(92)90048-r (1992).
54 Klinke, R. Neurotransmission in the inner ear. *Hear Res* **22**, 235-243, doi:10.1016/0378-5955(86)90100-0 (1986).
55 Jean, P., Ozcete, O. D., Tarchini, B. & Moser, T. Intrinsic planar polarity mechanisms influence the position-dependent regulation of synapse properties in inner hair cells. *Proc Natl Acad Sci U S A* **116**, 9084-9093, doi:10.1073/pnas.1818358116 (2019).
56 Sherrill, H. E. *et al.* Pou4f1 Defines a Subgroup of Type I Spiral Ganglion Neurons and Is Necessary for Normal Inner Hair Cell Presynaptic Ca(2+) Signaling. *J Neurosci* **39**, 5284-5298, doi:10.1523/JNEUROSCI.2728-18.2019 (2019).
57 Guinan, J. J., Jr. & Gifford, M. L. Effects of electrical stimulation of efferent olivocochlear neurons on cat auditory-nerve fibers. I. Rate-level functions. *Hear Res* **33**, 97-113, doi:10.1016/0378-5955(88)90023-8 (1988).
58 Winslow, R. L. & Sachs, M. B. Effect of electrical stimulation of the crossed olivocochlear bundle on auditory nerve response to tones in noise. *J Neurophysiol* **57**, 1002-1021, doi:10.1152/jn.1987.57.4.1002 (1987).
59 Felix, D. & Ehrenberger, K. The efferent modulation of mammalian inner hair cell afferents. *Hear Res* **64**, 1-5, doi:10.1016/0378-5955(92)90163-h (1992).
60 Maison, S. F. *et al.* Dopaminergic signaling in the cochlea: receptor expression patterns and deletion phenotypes. *J Neurosci* **32**, 344-355, doi:10.1523/JNEUROSCI.4720-11.2012 (2012).
61 Kujawa, S. G. & Liberman, M. C. Adding insult to injury: cochlear nerve degeneration after "temporary" noise-induced hearing loss. *J Neurosci* **29**, 14077-14085, doi:10.1523/JNEUROSCI.2845-09.2009 (2009).
62 Lauer, A. M., Fuchs, P. A., Ryugo, D. K. & Francis, H. W. Efferent synapses return to inner hair cells in the aging cochlea. *Neurobiol Aging* **33**, 2892-2902, doi:10.1016/j.neurobiolaging.2012.02.007 (2012).
63 Fernandez, K. A., Jeffers, P. W., Lall, K., Liberman, M. C. & Kujawa, S. G. Aging after noise exposure: acceleration of cochlear synaptopathy in "recovered" ears. *J Neurosci* **35**, 7509-7520, doi:10.1523/JNEUROSCI.5138-14.2015 (2015).
64 Knudson, I. M., Shera, C. A. & Melcher, J. R. Increased contralateral suppression of otoacoustic emissions indicates a hyperresponsive medial olivocochlear system in humans with tinnitus and hyperacusis. *J Neurophysiol* **112**, 3197-3208, doi:10.1152/jn.00576.2014 (2014).

65 Hua, Y., Laserstein, P. & Helmstaedter, M. Large-volume en-bloc staining for electron microscopy-based connectomics. *Nat Commun* **6**, 7923, doi:10.1038/ncomms8923 (2015).

66 Deerinck, T. J. *et al.* High-performance serial block-face SEM of nonconductive biological samples enabled by focal gas injection-based charge compensation. *J Microsc* **270**, 142-149, doi:10.1111/jmi.12667 (2018).

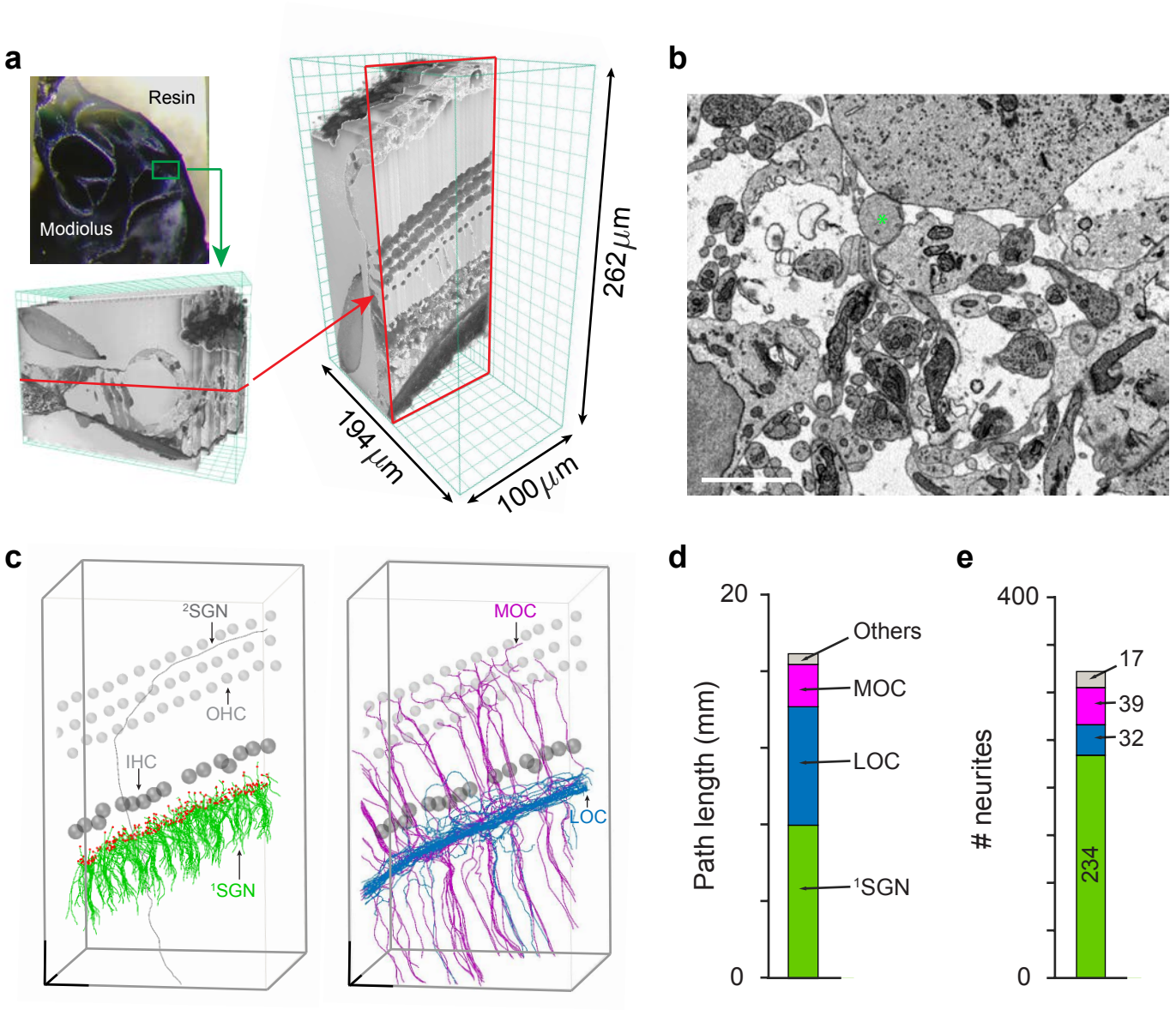
a
Resin
Modiolus
262 μm
194 μm
100 μm
b
c
²SGN
OHC
IHC
¹SGN
MOC
LOC
d
20
0
Path length (mm)
Others
MOC
LOC
¹SGN
e
400
0
neurites
17
39
32
234

Figure 1

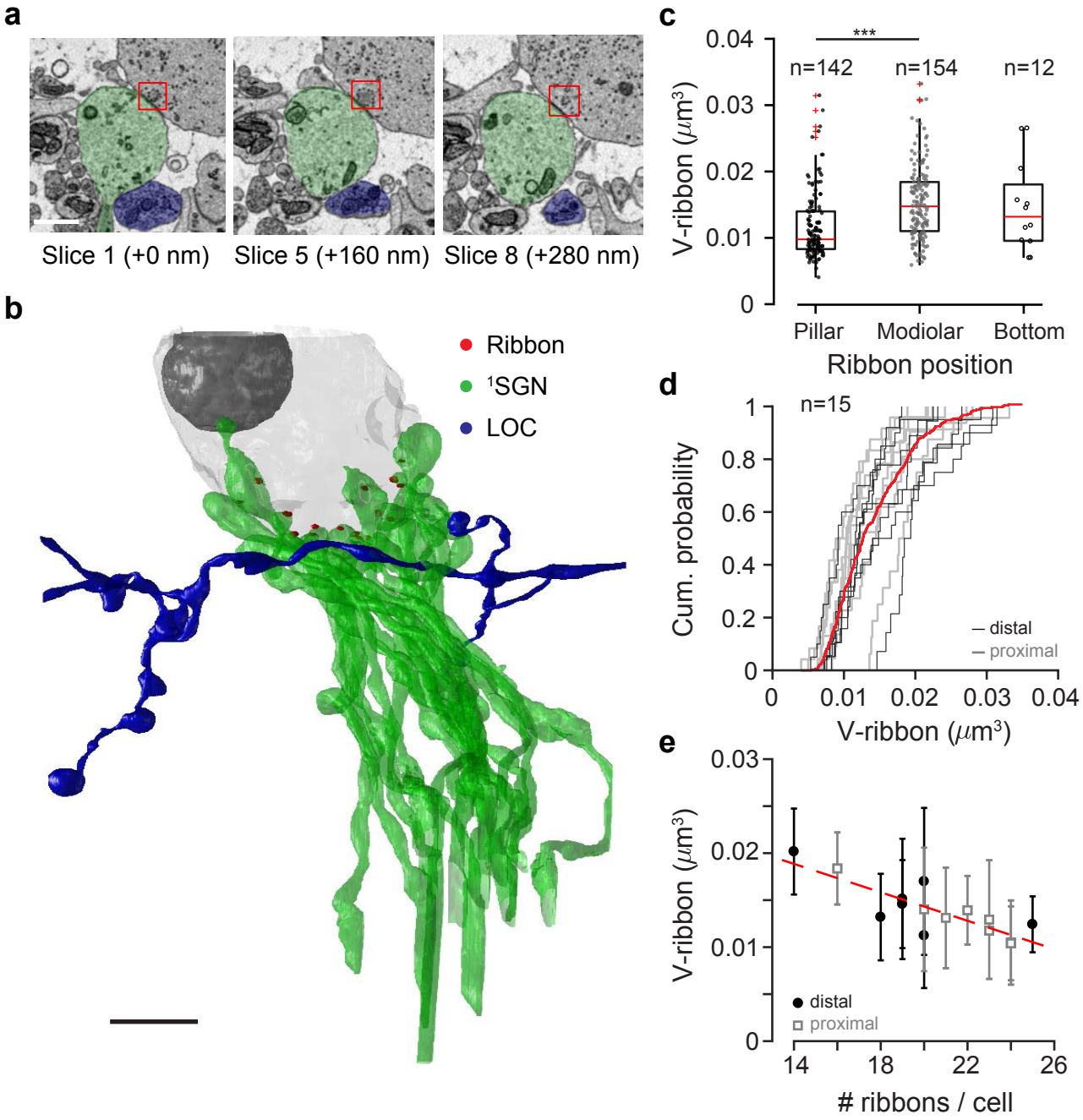
a
Slice 1 (+0 nm)
Slice 5 (+160 nm)
Slice 8 (+280 nm)
b
Ribbon
1SGN
LOC
c
***
n=142
n=154
n=12
V-ribbon (μm³)
0.04
0.03
0.02
0.01
0
Pillar
Modiolar
Bottom
Ribbon position
d
n=15
Cum. probability
1
0.8
0.6
0.4
0.2
0
distal
proximal
0
0.01
0.02
0.03
0.04
V-ribbon (μm³)
e
V-ribbon (μm³)
0.03
0.02
0.01
0
distal
proximal
14
18
22
26
ribbons / cell

Figure 2

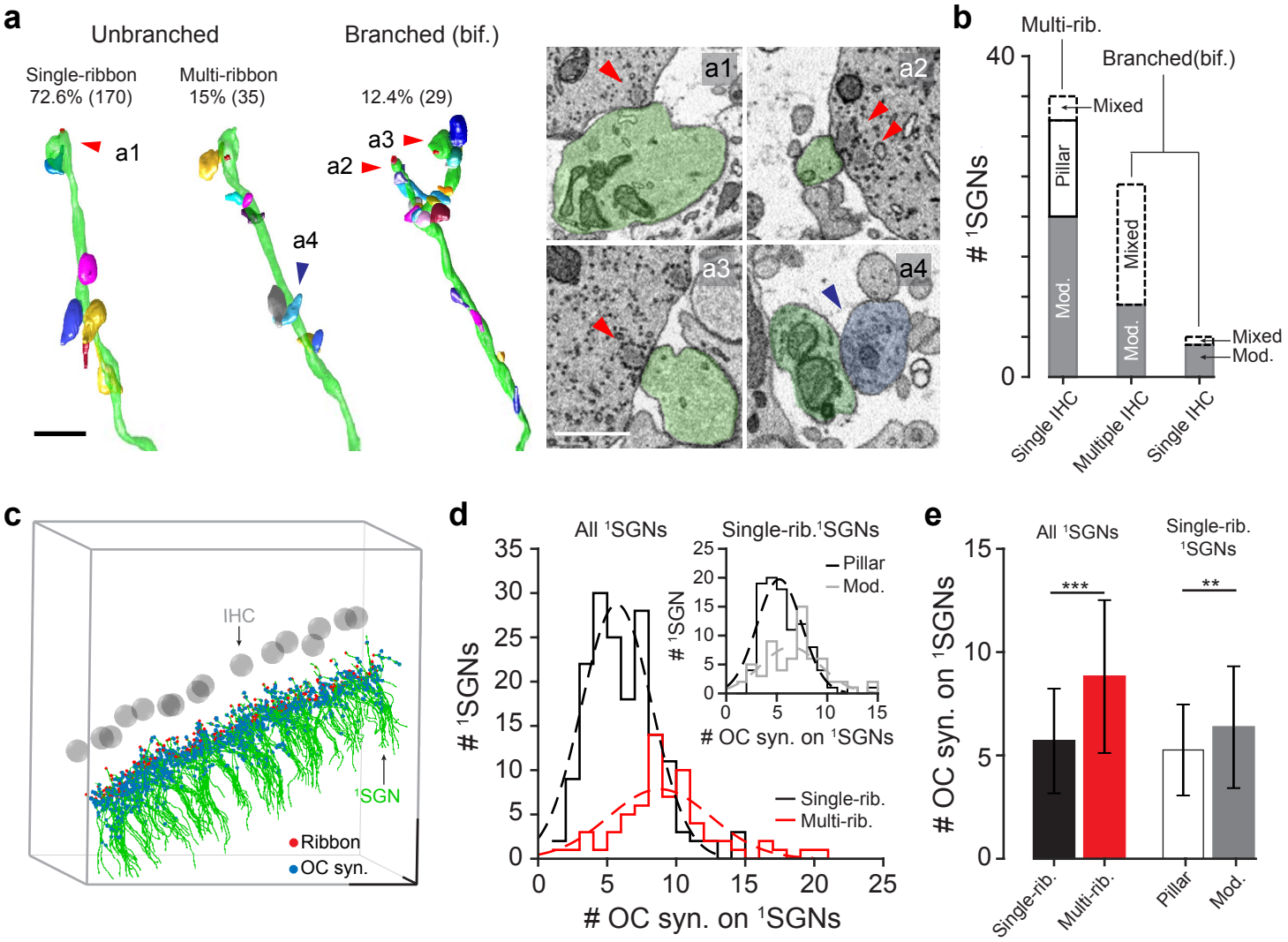
a
Unbranched
Branched (bif.)
Single-ribbon
72.6% (170)
Multi-ribbon
15% (35)
12.4% (29)
a1
a2
a3
a4
b
Multi-rib.
Branched(bif.)
Mixed
Pillar
Mod.
Mixed
Mod.
Mixed
Mod.
¹SGNs
40
0
Single IHC
Multiple IHC
Single IHC
c
IHC
¹SGN
Ribbon
OC syn.
d
All ¹SGNs
Single-rib.¹SGNs
Pillar
Mod.
¹SGN
OC syn. on ¹SGNs
Single-rib.
Multi-rib.
¹SGNs
OC syn. on ¹SGNs
e
All ¹SGNs
Single-rib.
¹SGNs
***
**
OC syn. on ¹SGNs
Single-rib.
Multi-rib.
Pillar
Mod.

Figure 3

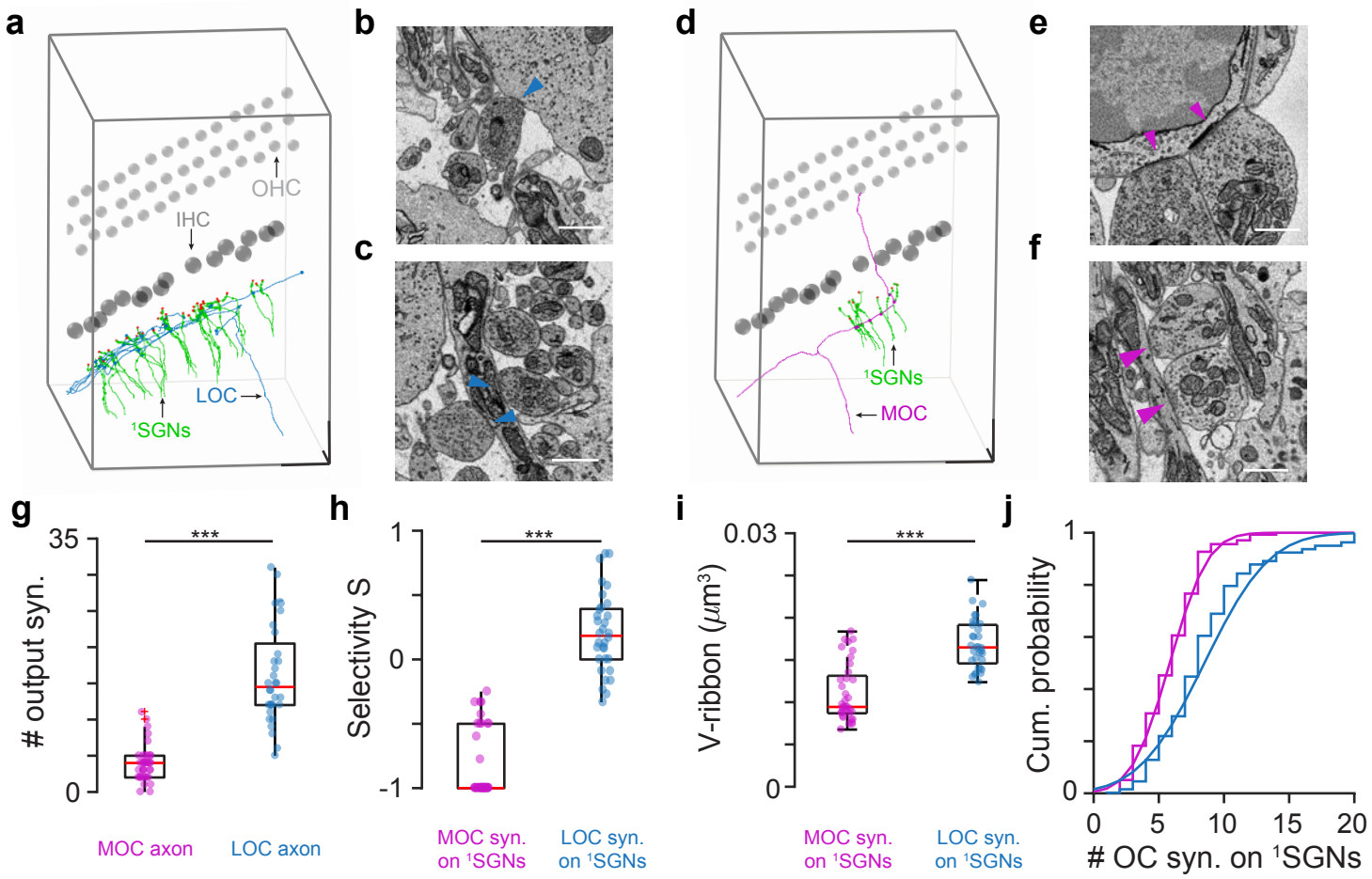
a
b
c
d
e
f
OHC
IHC
LOC
¹SGNs
¹SGNs
MOC
g
h
i
j
output syn.
35
0
***
MOC axon
LOC axon
Selectivity S
1
0
-1
***
MOC syn. on ¹SGNs
LOC syn. on ¹SGNs
V-ribbon (μm³)
0.03
0
***
MOC syn. on ¹SGNs
LOC syn. on ¹SGNs
Cum. probability
1
0
0
5
10
15
20
OC syn. on ¹SGNs

Figure 4

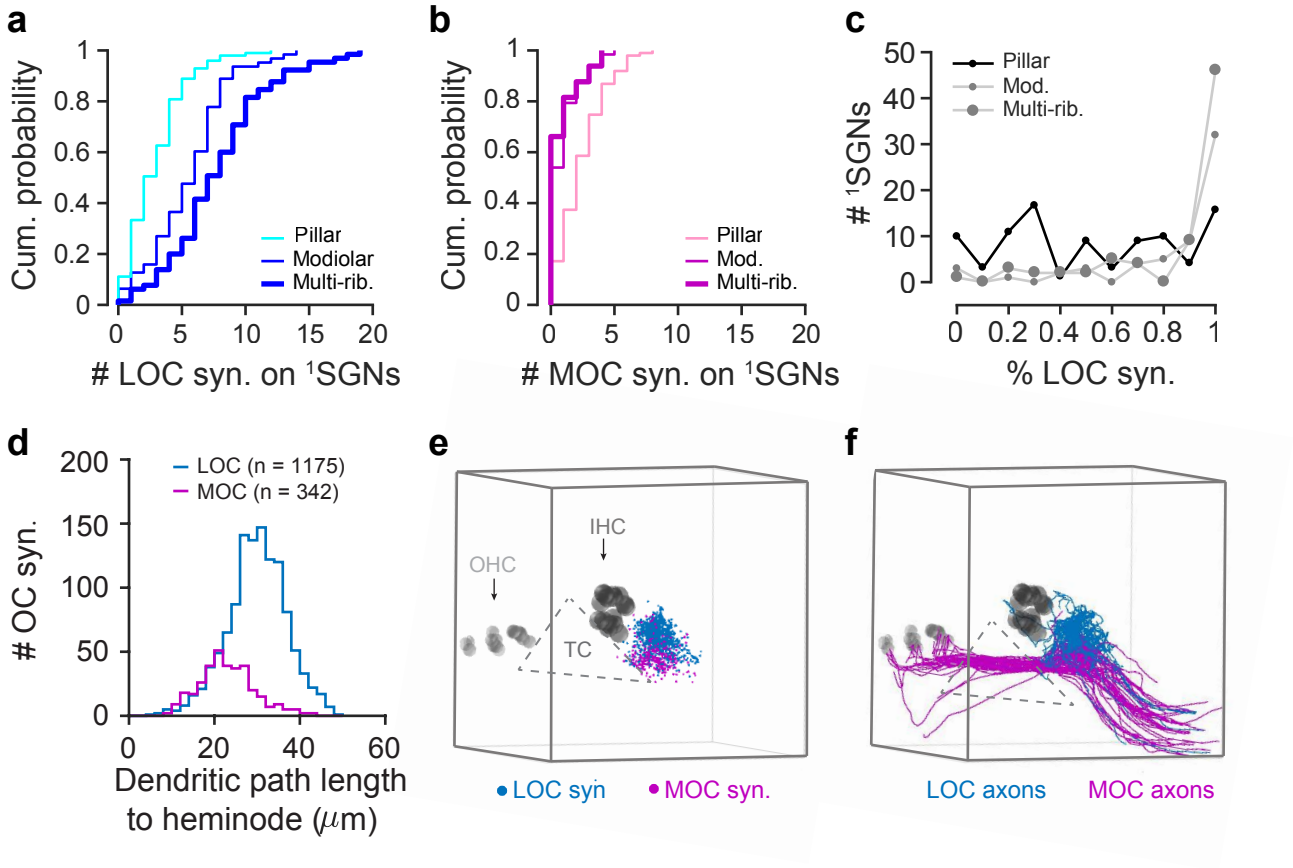
a
Cum. probability
Pillar
Modiolar
Multi-rib.
LOC syn. on ¹SGNs
b
Cum. probability
Pillar
Mod.
Multi-rib.
MOC syn. on ¹SGNs
c
¹SGNs
Pillar
Mod.
Multi-rib.
% LOC syn.
d
OC syn.
LOC (n = 1175)
MOC (n = 342)
Dendritic path length
to heminode (μm)
e
OHC
IHC
TC
LOC syn
MOC syn.
f
LOC axons
MOC axons

Figure 5

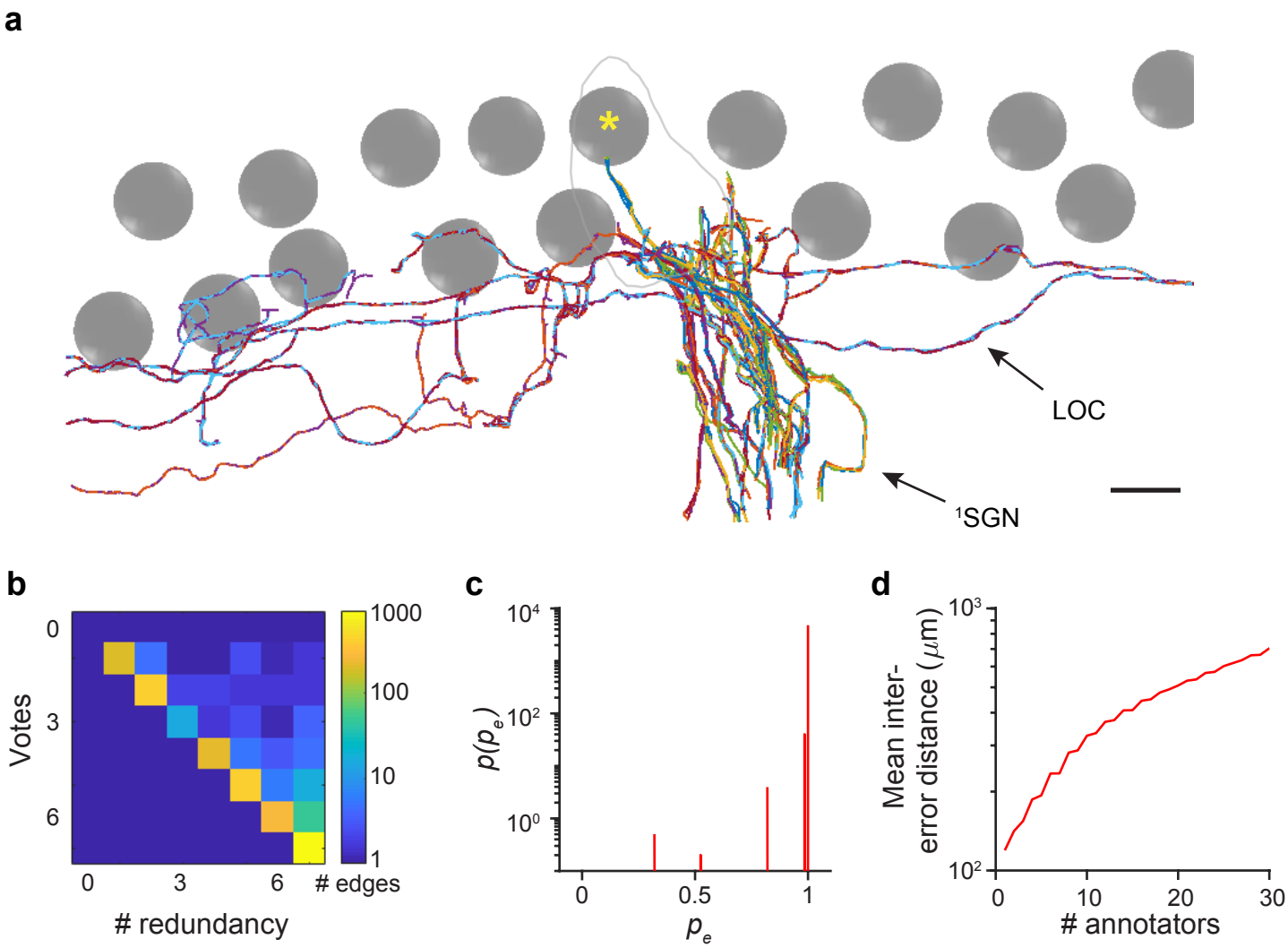
a
LOC
1SGN
b
Votes
0
3
6
redundancy
edges
1000
100
10
1
c
$p(p_e)$
10^4
10^2
10^0
0
0.5
1
p_e
d
Mean inter-error distance (μm)
10^3
10^2
0
10
20
30
annotators

Suppl. 1

[1]SGN-ID:

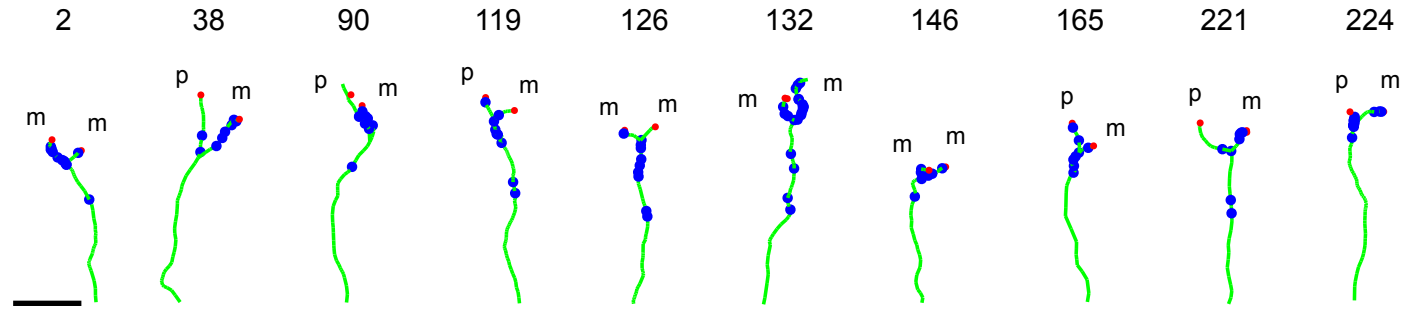

Suppl. 2

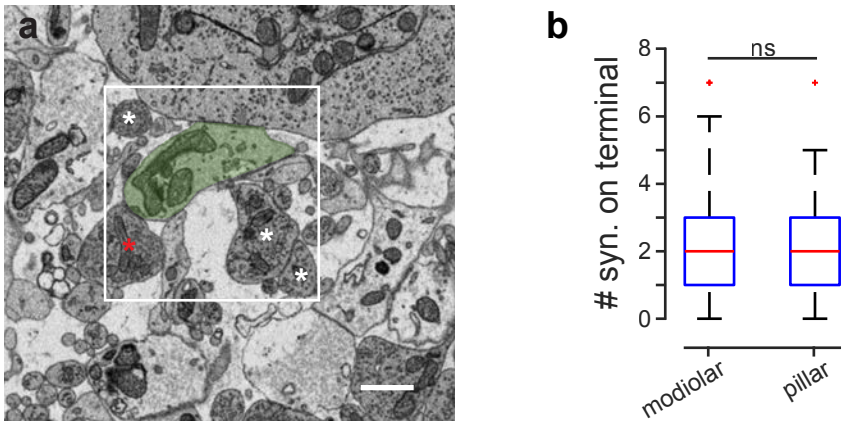

Suppl. 3